Focus Improvement of Highly Squinted Data Based on Azimuth Nonlinear Scaling

Guangcai Sun, Xiuwei Jiang, Mengdao Xing, *Member, IEEE*, Zhi-jun Qiao, Yirong Wu, *Member, IEEE*, and Zheng Bao, *Senior Member, IEEE*

Abstract—Since synthetic aperture technology was employed in radar signal processing, the information capability of radar has greatly been enhanced. A lot of imaging algorithms have also been developed. However, the high-resolution imaging for highly squinted synthetic aperture radar data is still a difficult issue due to large range migration and strong range dependence on the secondary range compression term that is relatively large and cubic with high focusing sensibilities for high resolution. To accommodate for this problem, the "squint-minimization" operation and azimuth nonlinear chirp scaling (CS) (ANCS) operation are studied in this paper. On the basis of these operations, we propose new imaging algorithms and analyze the characteristic of highly squinted data and the difficulty in focusing these data as well as discussing the principle of ANCS. We also introduce a new CS algorithm, and numerical examples show that the proposed algorithm is able to achieve 0.1 m of resolution under a squint angle as large as 70°s.

Index Terms—Azimuth nonlinear chirp scaling (CS) (ANCS), high resolution, high squint, radar imaging, synthetic aperture radar (SAR).

I. INTRODUCTION

IN RECENT years, there is a great development of the synthetic aperture radar (SAR). As an active sensor, SAR is able to work day and night under all weather conditions. In addition, SAR can operate at different frequencies and view angles in different polarimetric modes. This feature makes the SAR a flexible and effective tool for information retrieval

G. Sun, X. Jiang, and Z. Bao are with the National Key Laboratory of Radar Signal Processing, Xidian University, Xi'an 710071, China (e-mail: rsandsgc@126.com; jiang.xiuwei@zte.com.cn).

M. Xing is with the National Key Laboratory of Radar Signal Processing, Xidian University, Xi'an 710071, China, and also with the National Key Laboratory of Microwave Imaging Technology, Institute of Electronics, Chinese Academy of Sciences, Beijing 100080, China (e-mail: xmd@xidian.edu.cn).

Z. Qiao is with the Department of Mathematics, The University of Texas-Pan American, Edinburg, TX 78539-2999 USA (e-mail: qiao@utpa.edu).

Y. Wu is with the National Key Laboratory of Microwave Imaging Technology, Institute of Electronics, Chinese Academy of Sciences, Beijing 100080, China (e-mail: wyr@mail.ie.ac.cn).

Color versions of one or more of the figures in this paper are available online at http://ieeexplore.ieee.org.

Digital Object Identifier 10.1109/TGRS.2010.2102040

since the electromagnetic scattering property of a complex object varies with radar frequency, polarimetric mode, and incidence angle. The SAR is also capable of producing high-resolution images with high accuracy and has more and more applications.

The focusing of the SAR data is essentially a 2-D space-variant correlation of the received data with the point scatter response of the SAR data acquisition system. Although a 2-D space-variant correlator can handle the issue of SAR focusing, it is very inefficient in the processing of computation. Thus, various algorithms have been proposed in the past to make a better accuracy/efficiency tradeoff. The most popular algorithms are the range–Doppler (RD) algorithm [1]–[6], "wavenumber domain" or "ω–k" algorithm [7]–[13], [25], [26], and the chirp scaling (CS) algorithm [15], [16]. The RD algorithm uses the complicated interpolation scheme to accommodate the Doppler and range dependences of both the secondary range compression (SRC) term and the RCM [4]–[6]. Well-focused results can be obtained through using a long interpolator with range variance, which makes the algorithm less computationally efficient. The ω–k algorithm takes the data in the 2-D spectrum domain and gives good results by employing the so-called Stolt interpolation [13]. The CS algorithm employs the CS Theorem [14] to eliminate the range dependence of the *range migration* (RM) without any interpolation. This is implemented by multiplying the range uncompressed signal with a phase function so that the signal is compressed in range to a desired location [15], [16]. Without any interpolation in range cell migration correction (RCMC), the CS algorithm is effective and preserves the phase. Moreover, the CS algorithm is applicable to low-squint cases, e.g., less than 10°.

For high-squint cases, the traditional CS algorithm does not work anymore because it ignores the Doppler and range dependences of the SRC term. The focused results of the range marginal point suffer great degradation. The target's 2-D spectrum is skew and causes parts of the spectrum to cross into the adjacent pulse-repetition frequency (PRF) band [23]. The second problem can be accommodated by spectrum replicating and filtering [23]. An extended version of the CS algorithm, called ECS algorithm, was presented in literature [17]. The ECS is used to process the squint SAR data through eliminating spectrum folding caused by the traditional CS [15]. However, the method did not include the Doppler and range dependences of the SRC term and was limited for relatively lower squint cases. Moreira *et al.* [24] extended the ECS for 2-D scaling in the SAR and ScanSAR processing. In general, the Doppler

and range dependences on the SRC term and the cubic phase term must be taken into consideration for a better focused result in high-squint cases. Thus, the nonlinear CS (NCS) algorithm was proposed to deal with that problem [18]. Good results are achieved for squint angles up to 40° for the C-band and 30° for the L-band of SeaSat or the ERS-1 system.

All the aforementioned algorithms directly deal with the original squinted data and concentrate on how to analyze the characteristic of squinted data spectrum. However, the 2-D skew spectrum needs high PRF or extra computational load in the imaging processing due to the increased samples in azimuth [23] with a high squint and big bandwidth. Moreover, the degree of orthogonality between "range" and "azimuth" decreases where the cross terms are not ignorable. In this paper, we first "shear" the squinted spectrum and minimize the effect of squint. We call this procedure "squint minimization," which aims to increase the degree of orthogonality between the range and azimuth of the squinted data. The RM with its space variance, the SRC term, and the cubic phase are decreased much via the squint minimization.

Another method, based on the principle of the NCS, is adopted in [19] to equalize the frequency-modulation (FM) rate for the squint cases. In this method, the signal is first range compressed. Then, a linear RCMC is used to eliminate the RCM. After the correction, the FM rates of targets confined in a range gate will differ from each other. The NCS is used to focus the targets confined in a range gate. However, azimuth interpolation was required to eliminate the azimuth distortion; thus, the computational complexity increases. Furthermore, this method did not count the cubic phase term and its azimuth dependence. In our approach, we consider a nonlinear cubic phase that filters the operation to avoid the azimuth distortion and interpolation. In addition, the azimuth dependence of the cubic phase term is restricted to a given accuracy in our method (see the details in Appendix A).

This paper is organized as follows. Section II reviews the characteristic of the original and the "squint-minimized" data spectrum and introduces the principle of azimuth NCS (ANCS). Section III describes the "ANCS-based" CS algorithm and its application. Section IV gives the simulation results. Finally, in Section V, we give conclusions.

II. HIGHLY SQUINTED DATA ANALYSIS

A. Signal Model

A general form of the received signal is derived in terms of slant range and squint angle. With reference to the imaging geometry shown in Fig. 1, the slant range distance between the radar and a point target P is

$$R(t_m; R_0) = \sqrt{(vt_m - X_n)^2 + R_0^2 - 2R_0(vt_m - X_n)\sin\theta_0} \tag{1}$$

where v is the speed of the SAR platform, t_m is the slow time, R_0 is the slant range at the center of the aperture, θ_0 is the squint angle, and X_n indicates the target's azimuth position.
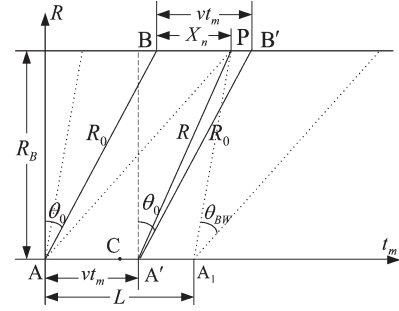
Fig. 1. Squinted-mode SAR geometry.

For further analysis, (1) is expanded to the Taylor's series

$$R(t_m; R_0) = R_0 - (vt_m - X_n)\sin\theta_0 + \frac{\cos^2\theta_0}{2R_0}(vt_m - X_n)^2$$
$$+ \frac{\sin\theta_0\cos^2\theta_0}{2R_0^2}(vt_m - X_n)^3 + \cdots$$
$$\approx \sqrt{R_0^2 + v^2\cos^2\theta_0\left(t_m - \frac{X_n}{v}\right)^2}$$
$$- \left(t_m - \frac{X_n}{v}\right)v\sin\theta_0$$
$$+ \frac{v^3\sin\theta_0\cos^2\theta_0}{2R_0^2}\left(t_m - \frac{X_n}{v}\right)^3 + \cdots. \tag{2}$$

The first row of (2) shows that the RM consists of range walk (e.g., linear term of slow time) and range curvature (e.g., quadratic term of slow time). The second row of (2) incorporates the quadratic range curvature into the square root term, which is similar to the form of RM in broadside SAR mode.

Assume that the transmitted waveform is given by

$$s_t(t_r) = a_r(t_r)\exp(j2\pi f_c t_r)\exp\left(j\pi\gamma t_r^2\right) \tag{3}$$

where $a_r(t_r)$ is the transmitted signal envelop, f_c is the carrier frequency, t_r denotes the fast time, and γ is the chirp rate. Then, the demodulated and normalized echoes from the target can be formulated as

$$s(t_r, t_m; R_0) = \exp\left[j\pi\gamma\left(t_r - \frac{2R(t_m; R_0)}{c}\right)^2\right]$$
$$\times \exp\left[-j\frac{4\pi}{\lambda}R(t_m; R_0)\right] \tag{4}$$

where c denotes the light speed and λ is the wavelength.

B. Spectrum of Highly Squinted Data

Taking 2-D fast Fourier transform (FFT) on both sides of (4) yields [18], [20]

$$S(f_r, f_a; R_B)$$
$$= \exp\left[-j\pi\frac{f_r^2}{\gamma}\right]\exp\left[-j2\pi f_a\left(t_c + \frac{X_n}{V}\right)\right]$$
$$\times \exp\left[j\phi_0(f_a; R_B) + j\phi_1(f_a; R_B)f_r\right.$$
$$\left. + j\phi_2(f_a; R_B)f_r^2 + j\phi_3(f_a; R_B)f_r^3 + \cdots\right] \tag{5}$$

where

$$
\begin{cases}
\phi_0(f_a; R_B) = -\frac{2\pi R_B}{v}\sqrt{f_{aM}^2 - f_a^2} \\
\phi_1(f_a; R_B) = -\frac{4\pi}{c}\frac{R_B}{\sqrt{1-(f_a/f_{aM})^2}} \\
\phi_2(f_a; R_B) = \pi R_B \frac{2\lambda \sin^2\theta}{c^2 \cos^3\theta} \\
\phi_3(f_a; R_B) = -\frac{2\pi R_B \lambda^2 \sin^2\theta}{c^3 \cos^5\theta}
\end{cases}
\tag{6a}
$$

$$
\begin{cases}
R_B = R_0 \cos\theta_0 \quad f_{\mathrm{dc}} = 2v\sin\theta_0/\lambda \\
f_{\mathrm{dc}} - B_a/2 \le f_a \le f_{\mathrm{dc}} + B_a/2 \quad f_{aM} = 2v/\lambda \\
\sin\theta = f_a/f_{aM} \quad \cos\theta = \sqrt{1-(f_a/f_{aM})^2}.
\end{cases}
\tag{6b}
$$

Each phase term is analyzed in the following.

1) The term $\phi_0(f_a; R_B)$ is the azimuth modulated term and should match for azimuth compression.
2) The term $\phi_1(f_a; R_B)$ contains the information of RM. From this term, we have the range delay carrying over into the RD domain

$$
R(f_a; R_B) = \frac{R_B}{\sqrt{1-(f_a/f_{aM})^2}} \triangleq R_B[1 + a(f_a)] \tag{7}
$$

where

$$
a(f_a) = \frac{1}{\sqrt{1-(f_a/f_{aM})^2}} - 1 \tag{8}
$$

is the migration factor. It shows that the Doppler domain is dependent on the signal trajectory. Moreover, $R(f_a; R_B)$ is a function of Doppler frequency f_a and the scatter's position R_B, showing the space variance of RM.

3) The term $\phi_2(f_a; R_B)$ shows the coupling of range and azimuth in the signal spectrum. It usually matches the SRC step in most algorithms, thus called the SRC term [4], [10]. The SRC term makes the chirp rate of the received signal unequal to γ, the original chip rate of the transmitted signal. The effective FM rate $\gamma_e(f_a, R_B)$ has the functional form

$$
\frac{1}{\gamma_e(f_a, R_B)} = \frac{1}{\gamma} - R_B\beta(f_a) \tag{9}
$$

where

$$
\beta(f_a) = \frac{2\lambda(f_a/f_{aM})^2}{c^2\left(\sqrt{1-(f_a/f_{aM})^2}\right)^3} = \frac{2\lambda\sin^2\theta}{c^2\cos^3\theta} \tag{10}
$$

is the range distortion factor. Range distortion is a direct consequence with only lack of orthogonality between range and azimuth for signal components away from zero Doppler. This distortion applies to any form of range modulation, not just to linear FM [15]. The higher the squint is, the larger the range distortion factor will be. The effective FM rate $\gamma_e(f_a, R_B)$ is a function of both Doppler and the scatter's position, showing its range dependence. As discussed before, for highly squinted data, $\gamma_e(f_a, R_B)$ changes a lot with range.

4) The term $\phi_3(f_a; R_B)$ is the coefficient of the cubic phase term of range frequency, which is not ignorable for squint angles as high as over 50°. It results from the lack of orthogonality between range and azimuth too. The other higher order terms (power is greater than three) are very small and thus ignorable.

C. Squint-Minimized or "Sheared" Spectrum of Highly Squinted Data

Some problems in high-squint SAR imaging arise from the lack of orthogonality between the range and azimuth of the SAR data. The azimuth spectrum is always partial folded [23] in the high-squint case. Spectrum extending was applied to eliminate the spectrum folding by replicating and filtering the spectrum [23].

The "squint minimization" aims to shear the data spectrum efficiently with little increase in computational load so that the orthogonality possibly increases.

The data in the $f_r - t_m$ domain (f_r is range frequency and t_m is slow time) are formulated as

$$
S(f_r, t_m; R_0) = \exp\left[-j\pi\frac{f_r^2}{\gamma}\right]
$$
$$
\times \exp\left[-j\frac{4\pi}{c}R(t_m; R_0)(f_r + f_c)\right]. \tag{11}
$$

Now, we construct a function

$$
H_{\mathrm{shear}}(f_r, t_m; R_0) = \exp\left[-j2\pi f_{\mathrm{dc}}(1 + f_r/f_c)t_m\right] \tag{12}
$$

where $f_{\mathrm{dc}} = 2v\sin\theta_0/\lambda$ is the Doppler center.

Then, the constructed function is multiplied by $S(f_r, t_m; R_0)$. Note that this operation introduces a Doppler shift linear to range frequency. This feature decreases the coupling or increases the orthogonality between range and azimuth, which will be addressed in the following.

After the multiplication, the data are transformed into the 2-D frequency domain with the azimuth FFTs, and thus, the new data spectrum becomes

$$
S(f_r, f_a; R_0)
$$
$$
= \exp\left[-j\frac{4\pi}{c}(f_r + f_c)X_n\sin\theta_0\right]
$$
$$
\times \exp\left[-j2\pi f_a\frac{X_n}{V}\right]\exp\left[j\phi_{0\mathrm{new}}(f_a; R_0)\right]
$$
$$
\times \exp\left\{j\left[\phi_{1\mathrm{new}}(f_a; R_0)f_r + \phi_{2\mathrm{new}}(f_a; R_0)f_r^2\right.\right.
$$
$$
\left.\left. + \phi_{3\mathrm{new}}(f_a; R_0)f_r^3 + \cdots\right]\right\} \tag{13}
$$

where

$$
\begin{cases}
\phi_{0\mathrm{new}}(f_a; R_0) = -\frac{2\pi R_0}{v\cos\theta_0}\sqrt{f_{aM}^2 - f_a^2} \\
\qquad\qquad + \frac{2\pi R_0\tan\theta_0\sin^3\theta}{\lambda\cos^3\theta} \\
\phi_{1\mathrm{new}}(f_a; R_0) = -\frac{4\pi}{c}R_0[1 + a_{\mathrm{new}}(f_a)] \\
\phi_{2\mathrm{new}}(f_a; R_0) = -\frac{\pi}{\gamma_{e,\mathrm{new}}(f_a, R_0)} \\
\phi_{3\mathrm{new}}(f_a; R_0) = -\frac{2\pi R_0\lambda^2\sin^2\theta}{c^3\cos^5\theta}\rho(f_a)
\end{cases}
\tag{14a}
$$

$$\begin{cases} \frac{1}{\gamma_{e,\text{new}}(f_a,R_B)} = \frac{1}{\gamma} - R_0\beta_{\text{new}}(f_a) \\ -\frac{B_a}{2} \leq f_a \leq \frac{B_a}{2} \\ f_{aM} = \frac{2v\cos\theta_0}{\lambda} \quad \sin\theta = \frac{f_a}{f_{aM}} \\ \cos\theta = \sqrt{1 - \left(\frac{f_a}{f_{aM}}\right)^2} \end{cases} \quad (14b)$$

$$\begin{cases} a_{\text{new}}(f_a) = \frac{1}{\cos\theta} - \frac{\tan\theta_0\sin^3\theta(\cos^2\theta-3)}{2\cos^5\theta} - 1 \\ \beta_{\text{new}}(f_a) = \frac{2\lambda\sin^2\theta}{c^2\cos^3\theta}\left[1 + \frac{3\tan\theta_0\sin\theta(2+3\sin^2\theta)}{2\cos^4\theta}\right] \\ \rho(f_a) = 1 - \frac{\tan\theta_0\sin\theta(30\cos^2\theta-3\cos^4\theta-35)}{2\cos^4\theta}. \end{cases} \quad (14c)$$

We use subscript "new" to distinguish from the primary corresponding parameters used in the analysis of the original data spectrum. Note that the interval of Doppler frequency changes from $f_{\text{dc}} - B_a/2 \leq f_a \leq f_{\text{dc}} + B_a/2$ to $-B_a/2 \leq f_a \leq B_a/2$. The new phase terms are as follows.

1) $\phi_{0\text{new}}(f_a; R_0)$ showing the new azimuth modulation and matching for azimuth compression.
2) $\phi_{1\text{new}}(f_a; R_0)$ indicating the new RM. The migration factor $a_{\text{new}}(f_a)$ is formulated in (14c).
3) $\phi_{2\text{new}}(f_a; R_0)$, new range modulation, featured by the new range distortion factor $\beta_{\text{new}}(f_a)$, as shown in (14c).
4) $\phi_{3\text{new}}(f_a; R_0)$ showing the new cubic phase term.

Range extension is a problem brought by squint minimization. One can detail the range extension sampling number. $\phi_{1\text{new}}(f_a; R_0)f_r$ in (13) can express the new RCM after squint minimization, and the new migration factor $a_{\text{new}}(f_a)$ determines the variation of the RCM with f_a. By using squint minimization, the linear part within the original migration factor is eliminated. Therefore, one can express the range extension using original linear RCM approximately. Supposing M, N, and N_{ext} denote the original azimuth, range, and range extension sampling numbers, respectively, N_{ext} can be expressed as

$$N_{\text{ext}} = \left(v\frac{M}{PRF}\sin\theta_0\right) \Big/ \left(\frac{C}{2F_s}\right) \quad (15)$$

where PRF and F_s denote the azimuth and range sampling frequency, the numerator denotes the linear RCM, and the denominator denotes the range sampling interval. The range extension will be large when the azimuth sampling number is big. Therefore, in order to reduce the computational load brought by range extension, it is necessary to make blocks in the azimuth. In order to increase the efficiency in imaging processing, the azimuth subblock should be greater than an azimuth aperture.

D. Difference Between the Original and the Squint-Minimized Spectrum

To show the difference between the original and the squint-minimized spectrum, some numerical examples are given in this section. The simulation parameters are listed in Table I.

The "squinted" and squint-minimized data spectra are shown in Fig. 2. We can see from Fig. 2 that the raw data spectrum is highly squinted at the squint angle of $45°$ while the orthogonality between the range and azimuth is much increased

TABLE I
PARAMETERS FOR SIMULATION

Wavelength	0.2 m	Bandwidth	150 MHz	Sampling Frequency	180 MHz
Pulse Width	2.5 μs	velocity	100 m/s	Aperture Time	11.32 s
Squint angle	45 deg	PRF	88.4 Hz	Slant distance	8 km

after the squint minimization. We call the new spectrum squint-minimized or sheared spectrum.

Now, we examine the characteristic of the squint-minimized spectrum by evaluating the space variance of RM and effective FM rate, as well as the cubic phase term.

We know from (7) that $R(f_a; R_B)$ is a function of both f_a and R_B, manifesting the Doppler and range dependences on RM. Taking partial derivative with respect to R_B in (8) yields

$$\partial R(f_a; R_B)/\partial R_B = 1 + a(f_a). \quad (16)$$

Thus, RM factor, i.e., $a(f_a)$, could be employed to evaluate the range dependence on RM. The larger the RM factor is, the larger the range dependence on RM will be. According to the parameters in Table I, the RM factor of the raw data spectrum and squint-minimized data spectrum is shown in Fig. 3(a). The RM factor of the squint-minimized data is only a few thousandths of the original raw data, which shows that the space variance of RM is greatly decreased by squint minimization.

As discussed earlier, the space variance of the effective FM rate $\gamma_e(f_a, R_B)$ [see (9) and (14)] is another problem for the highly squinted SAR imaging. However, the space variance of $\gamma_e(f_a, R_B)$ is much reduced by the squint-minimization operation. To see this, the Doppler band-unified difference of $\gamma_e(f_a, R_B)$ between arbitrary range R and reference range R_{ref} is defined by

$$\xi(R) = \frac{1}{B_a}\sum_{f_a}|\gamma_e(f_a, R) - \gamma_e(f_a, R_{\text{ref}})| \quad (17)$$

where B_a denotes the Doppler bandwidth.

The common logarithmic diagram of $\xi(R)$ with respect to R is shown in Fig. 3(b1)–(b2), with the squint angle being $60°$ and $70°$, respectively. From those figures, the variation of $\gamma_e(f_a, R_B)$ is greatly decreased for the squint-minimized data.

Let us now discuss the issue of the large cubic phase terms. The cubic phase terms of the original and squint-minimized data are formulated in (6a) and (14a), respectively.

Let

$$K_1(f_a) = -\frac{\phi_3(f_a; R_0)}{2\pi R_0} \quad K_2(f_a) = -\frac{\phi_{3\text{new}}(f_a; R_0)}{2\pi R_0}. \quad (18)$$

Then, $K_1(f_a)$ and $K_2(f_a)$ show the variation of $\phi_3(f_a; R_0)$ in f_a, as well as the rate of $\phi_3(f_a; R_0)$ with range. To show the effect of squint minimization on the cubic phase term, we plot the diagram of $K_1(f_a) \sim f_a$ and $K_2(f_a) \sim f_a$ in Fig. 3(c). The value of $K_2(f_a)$ is only several parts of $K_1(f_a)$ in terms of 10^5, which implies that the cubic phase and its variance are greatly reduced by the squint minimization. Since the squint minimization provides us a new 2-D spectrum, we introduce a new imaging method in the next section, which is called the ANCS-based CS algorithm.
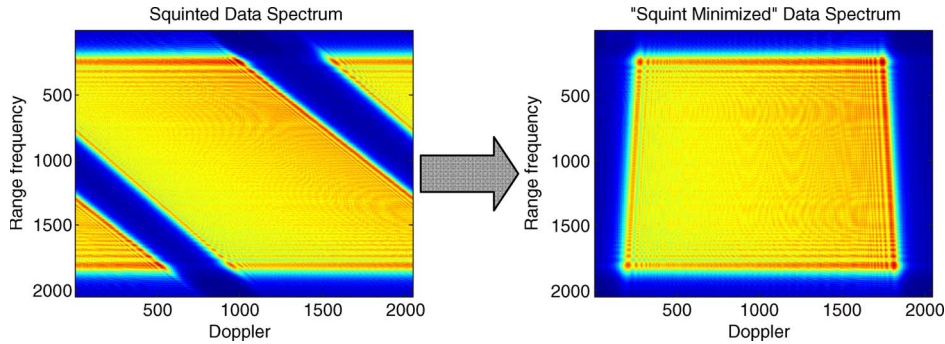
Fig. 2.   Spectrum of raw data and squint-minimized data.
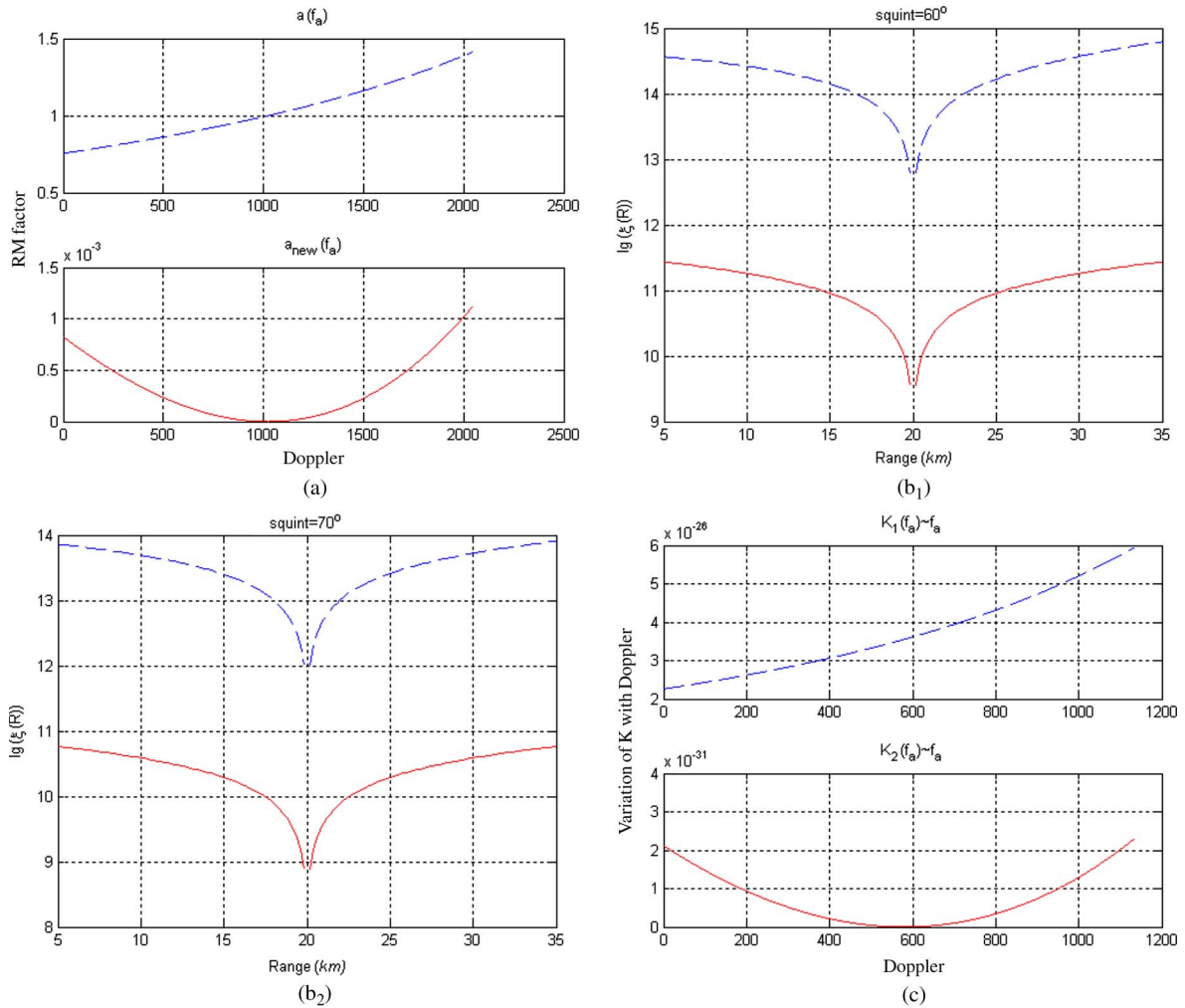
Fig. 3.   Diagrams for spectrum characteristic evaluation. (a) RM factor. (b1)–(b2) Space variance of effective FM rate. (c) Diagram of cubic phase term. The dotted and solid lines denote the parameters corresponding to the original and the squint-minimized raw data spectrum, respectively.

III. SAR IMAGING ALGORITHM BASED ON SQUINT MINIMIZATION AND ANCS

The new CS algorithm is addressed in this section. The ANCS and squint minimization are incorporated into the algorithms. The flow chart of the ANCS-based CS algorithm is shown in Fig. 4. In the CS algorithm, one takes into consideration of the range dependence of RM. The range dependence of RM is eliminated by the CS operation without interpolation. Thus, the CS algorithm is very efficient and precise in RM

correction. However, we know that the cubic phase term is neglected in the presented CS algorithm and the effective FM rate is evaluated at the reference range R_{ref} in the scaling function [see (19)] and the range compression function [see (21)]. The reason is that the cubic phase term is largely reduced by the squint minimization and so is the range dependence of the effective FM rate. Thus, the new CS algorithm is still precise enough in high-squint SAR applications and can perform better than the conventional CS algorithm in [15].
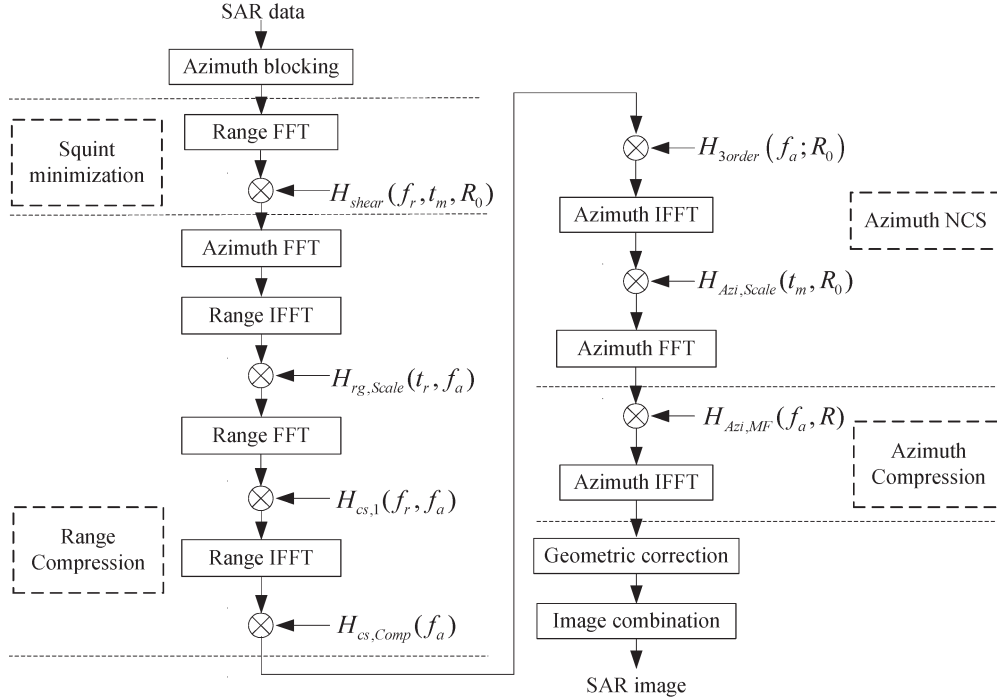
Fig. 4. Flow chart of the ANCS-based CS algorithm.

A. CS for RCMC

By performing inverse FFT (IFFT) on f_r in (13), we get the squint-minimized signal in the $t_r - f_a$ domain (t_r denotes fast time). Since the expression has much difference from the traditional one, it is necessary to exploit new imaging algorithms. Due to the interpolation needed in the RD algorithm to accommodate the range and Doppler dependence of the RCM term, the CS algorithm, using the CS Theorem, is more popular to substitute interpolation by FFT. Here, we use the CS algorithm to deal with the range dependence of RM.

We construct a quadratic phase function to "scale" the signal

$$
H_{rg,\text{Scale}}(t_r, f_a) = \exp\left[j\pi\gamma_{e,\text{new}}(f_a; R_{\text{ref}})a_{\text{new}}(f_a) \right.
$$
$$
\left. \times \left(t_r - \frac{2R(f_a; R_{\text{ref}})}{c} \right)^2 \right] \quad (19)
$$

where $H_{rg,\text{Scale}}(t_r, f_a)$ is multiplied by the squint-minimized signal in $t_r - f_a$ domain, called the *CS* operation. By ignoring the constant phase term, the signal can be written as

$$
S(t_r, f_a; R_0)
$$
$$
\approx \exp\left\{ -j\pi\left(1 + a_{\text{new}}(f_a)\right)\gamma_{e,\text{new}}(f_a; R_{\text{ref}}) \right.
$$
$$
\times \left[t_r - \frac{2\left(R_0 + R_{\text{ref}}a_{\text{new}}(f_a)\right)}{c} - \frac{2X_n \sin\theta_0}{c} \right]^2 \right\}
$$
$$
\times \exp\left[j\phi_{0\text{new}}(f_a; R_0) \right] \exp\left[-j2\pi f_a \frac{X_n}{V} \right]. \quad (20)
$$

Clearly, the spatial variance of RM is eliminated in (20). The signal is transformed into the $f_r - f_a$ domain.

A function is now constructed for range matched filtering (MF) and RM correction

$$
H_{\text{cs},1}(f_r, f_a) = \exp\left[j\pi \frac{1}{\gamma_{e,\text{new}}(f_a, R_{\text{ref}})\left[1 + a_{\text{new}}(f_a)\right]} f_r^2 \right]
$$
$$
\times \exp\left[j4\pi \frac{R_{\text{ref}}a_{\text{new}}(f_a)}{c} f_r \right]. \quad (21)
$$

The function is multiplied by the FFT expression of (20), and then, performing IFFT on f_r completes the range compression. By substituting R by $R_0 + X_n \sin\theta_0$, the range-compressed signal is expressed as follows:

$$
S(t_r, f_a; R_0) = \delta\left(t_r - \frac{2}{c}R \right) \exp\left(-j\Theta_\Delta(f_a; R_0) \right)
$$
$$
\times \exp(j\phi_{0\text{new}}) \exp\left[-j\frac{2\pi f_a X_n}{V} \right] \quad (22)
$$

where

$$
\Theta_\Delta(f_a; R_0) \approx \frac{4\pi}{c^2}\gamma_{e,\text{new}}(f_a; R_{\text{ref}})a_{\text{new}}(f_a)
$$
$$
\times \left[1 + a_{\text{new}}(f_a)\right](R - R_{\text{ref}})^2. \quad (23)
$$

Equation (23) shows the residue phase caused by the *CS* operation. The imagery point is located at $R_0 + X_n \sin\theta_0$ from (22). From (23), the residue phase $\Theta_\Delta(f_a; R_0)$ can be calculated according to the range cells after range compression. Therefore, a function for the phase compensation is given through

$$
H_{\text{cs,Comp}}(f_a) = \exp\left[j\Theta_\Delta(f_a; R_0) \right]. \quad (24)
$$

This is multiplied by (23) to remove the residue phase term induced by the CS operation.

B. ANCS

As pointed out earlier, the squint minimization results in the inequality of the Doppler rate of the scatters in the same range cell after range compression, which needs special consideration. Hence, the ANCS operation is proposed to solve this problem.

Starting from (22) and ignoring the unimportant constant phase term, we can have the signal approximately equal to

$$S(t_r, f_a; R_0) = \delta\left(t_r - \frac{2}{c}R\right) \exp\left(-j\frac{\Omega_a^2}{2b_m}\right)$$

$$\times \exp\left(j\frac{d_m}{b_m^3}\Omega_a^3\right) \exp\left[-j\Omega_a\frac{X_n}{V}\right] \quad (25)$$

where

$$\begin{cases} \Omega_a = 2\pi f_a \\ b_m = -4\pi v^2 \cos^2\theta_0/(\lambda R_0) \\ d_m = -2\pi v^3 \sin\theta_0 \cos^2\theta_0 \lambda/R_0^2. \end{cases} \quad (26)$$

From (20), we know that the imagery point is at R, while the scatter's actual position is at R_0. Moreover, the parameters for azimuth compression, i.e., b_m and d_m, are functions of the scatter's actual position R_0. However, they are calculated according to imagery point's position R rather than R_0 during azimuth processing and therefore cause azimuth defocusing. Hence, a special processing is required to avoid azimuth defocusing. A method, based on the principle of NCS, was proposed in [19] to equalize the azimuth FM rate. However, unfortunately, the introduction of *perturbation function* resulted in azimuth distortion. Thus, an azimuth interpolation was required, but increased the computational complexity and loss in phase property. In this paper, another ANCS is employed. First, we construct a cubic phase function to avoid the azimuth distortion

$$H_{3\text{order}}(f_a; R_0) = \exp\left(jd_m'\Omega_a^3\right)\exp\left(-j\frac{d_0}{b_0^3}\Omega_a^3\right) \quad (27)$$

where d_0 and b_0 are the values of b_m and d_m, respectively, when $R_0 = R$. Equation (27) is multiplied by (25). This step is called *azimuth cubic phase filtering*. After this step, the signal is transformed into the azimuth time domain via taking IFFT on Ω_a using the stationary phase method. Thus, we have

$$S(t_r, t_m; R_0) = \delta\left(t_r - \frac{2}{c}R\right) \exp\left[j\frac{b_m}{2}\left(t_m - \frac{X_n}{v}\right)^2\right.$$

$$\left. + j\left(d_m' + \frac{d_m}{b_m^3} - \frac{d_0}{b_0^3}\right)b_m^3\left(t_m - \frac{X_n}{v}\right)^3\right]. \quad (28)$$

Now, the azimuth scaling function is created

$$H_{\text{Azi,Scale}}(t_m, R_0) = \exp\left(jq_2 t_m^2/2\right)\exp\left(jq_3 t_m^3\right). \quad (29)$$

It is multiplied by $S(t_r, t_m; R_0)$ on both sides of (28). This step is called *ANCS*.

After the ANCS is performed, the signal is transformed to the Doppler domain via the stationary phase method. Then, we have

$$S(t_r, f_a; R_0) = \delta(t_r - 2R/c)\exp\left[j\Phi(f_a)\right] \quad (30)$$

where $\Phi(f_a)$ is the phase term in the azimuth frequency domain. b_m and d_m are evaluated according to the imagery point's position rather than the scatter's actual position. Therefore, they are approximately equal to

$$b_m \approx b_0 + b_1\tau \quad (31)$$
$$d_m \approx d_0 + d_1\tau \quad (32)$$

where $\tau = X_n/v$ denotes the *azimuth center time* of the point, b_0 and d_0 are the same as the ones in (22), and b_1 and d_1 are the ratios of b_m and d_m varying with τ. The approximations (31) and (32) hold when the azimuth scope of the observed scene is very small comparing with the slant range. Using (31) and (32), we obtain

$$\Phi(f_a) \approx A + B\tau f_a + C\tau^2 f_a + D\tau f_a^2 + E\tau f_a^3 \ldots \quad (33)$$

where A is the azimuth unvarying term, the second term stands for the azimuth position, the third one represents the azimuth distortion, the fourth one denotes the azimuth dependence on the azimuth FM, and the last one refers to the azimuth dependence on the cubic phase term. In order to eliminate the azimuth distortion and azimuth dependence on azimuth FM, we usually set the third and fourth terms to be zeros. Also, we are willing to focus the point target; hence, we choose B to be equal to a constant. Therefore, we have

$$B = -2\pi/\beta_{\text{scl}} \quad C = 0 \quad D = 0 \quad (34)$$

where β_{scl} is the azimuth scaling factor and its selection will be determined in the following. As shown in Appendix A, we may have the following parameters:

$$d_m' = \frac{(\beta_{\text{scl}} - 0.5)b_1}{3(\beta_{\text{scl}} - 1)b_0^3} \quad q_2 = b_0(\beta_{\text{scl}} - 1) \quad q_3 = \frac{(\beta_{\text{scl}} - 1)b_1}{6}. \quad (35)$$

Thus, the signal in the $t_r - f_a$ domain now becomes

$$S(t_r, f_a; R) = \delta\left(t_r - \frac{2R}{c}\right)$$

$$\times \exp\left(-j\frac{2\pi X_n f_a}{v\beta_{\text{scl}}} - j\frac{2\pi^2 f_a^2}{\beta_{\text{scl}} b_0}\right.$$

$$\left. + j\frac{4\pi^3 b_1 f_a^3}{3\beta_{\text{scl}}(\beta_{\text{scl}} - 1)b_0^3} + j\phi_{\text{con}}\right) \quad (36)$$
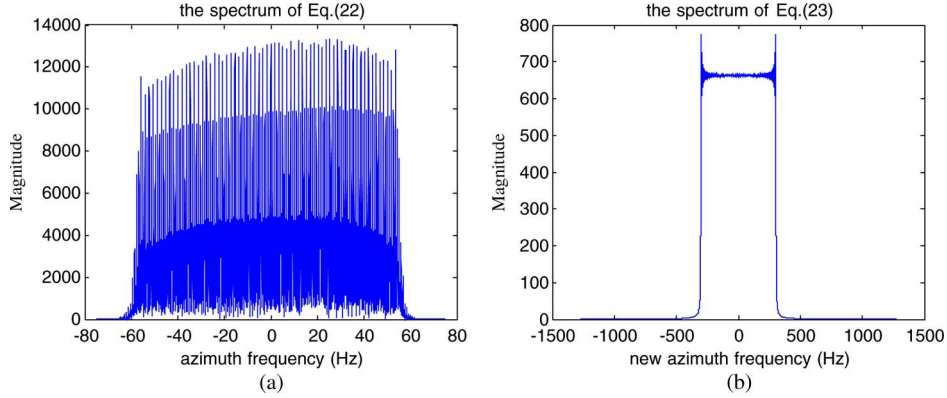
Fig. 5. Spectrum of (23) and (24). (a) Spectrum of (23) with the old PRF. (b) Spectrum of (24) with the new PRF.

where ϕ_{con} denotes the independent phase term of the azimuth frequency. The quadratic and cubic phase terms of f_a are related to the azimuth phase modulation. Apparently, the azimuth modulation is independent of the scatter's azimuth position due to the *ANCS*. Thus, a uniform azimuth *MF* function is obtained

$$H_{\mathrm{Azi,MF}}(f_a, R) = \exp\left(j\frac{2\pi^2 f_a^2}{\beta_{\mathrm{scl}} b_0} - j\frac{4\pi^3 b_1 f_a^3}{3\beta_{\mathrm{scl}}(\beta_{\mathrm{scl}} - 1)b_0^3}\right). \tag{37}$$

The signal in (36) is multiplied by the *MF* function on both sides of (37) and then transformed back into the azimuth time domain to complete the azimuth compression. The result after azimuth compression is

$$S(t_r, t_m; R_0) = \delta\left(t_r - \frac{2(R_0 + X_n \sin\theta_0)}{c}\right)$$

$$\times \delta\left(t_m - \frac{X_n/\beta_{\mathrm{scl}}}{v}\right)\exp(j\phi_{\mathrm{con}}) \tag{38}$$

where the position of the imagery point is located at $(X_n/\beta_{\mathrm{scl}}, R_0 + X_n \sin\theta_0)$, while the scatter's actual position is (X_n, R_0) in "acquisition Doppler output geometry" [15] or $(R_0 \sin\theta_0 + X_n, R_B)$ in "zero Doppler output geometry" [15]. Thus, the geometrical distortion is introduced by the squint minimization and *ANCS*. The geometrical correction may be needed according to the practical requirements.

C. Some Considerations of the Application

1) Scaling Factor β_{scl}: β_{scl} is an azimuth scaling factor. After azimuth compression, the position of the point is located at X_n/β_{scl}. The optimal selection of β_{scl} can be figured out (see details in Appendix B). However, if the optimal value of β_{scl} is big, another problem will arise. Equation (29) is involved in a quadratic phase term, which indicates a bandwidth signal in the spectrum domain. When (29) is multiplied by (28) in the time domain, the total bandwidth is widened. Once the equivalent bandwidth outclasses the PRF, the spectrum is folded.

In fact, the spectrum of (28) is restricted in $[-PRF/2 \quad PRF/2]$. The spectrum of a given expression (28)
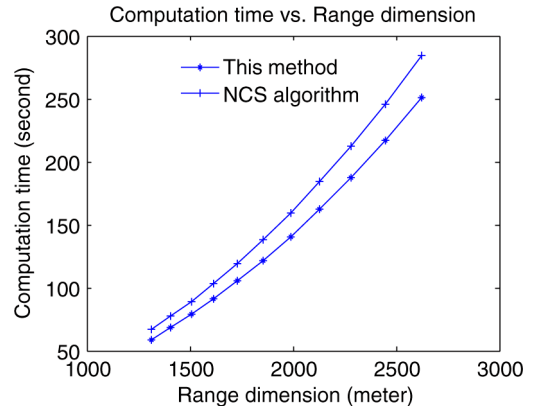
Fig. 6. Computational time versus range dimension with different algorithms.

TABLE II
SIMULATION PARAMETERS

wavelength	0.01 m	Bandwidth	1.5 GHz	Sampling frequency	1.8 GHz
Pulse width	2.5 μs	velocity	100 m/s	Azimuth aperture length	0.2 m
Squint angle		PRF			
50 deg		803.5 Hz		Reference range	15 km
60 deg		625.0 Hz			
70 deg		427.5 Hz			

is not folded if we adopt a higher PRF, namely, PRF1. Thus, the spectrum of (30) is confined in $[-PRF1/2 \quad PRF1/2]$. Fig. 5 shows the problem and corresponding countermeasure. From Fig. 5(b), we see that the spectrum must be folded with the old PRF while the spectrum is not folded with the new PRF1. On the other side, the extension of (28) is carried out by appending zeros in the frequency domain. Then, the multiplication of (28) and (29) is carried out in the time domain. After this multiplication, we intercept the corresponding part of the spectrum as the result of (30) to resume the old PRF.

2) Motion Compensation in Image Processing: A two-step motion compensation method was applied in the ECS algorithm to process squint SAR data [17]. For the airborne case, the first step is to define the phase error correction for a reference range,

TABLE III
SIMULATION RESULTS OF PROPOSED CS ALGORITHM

Squint angle(deg.)	R-Rref	Range resolution(m)	Azimuth resolution(m)	PSLR(dB) (range)	ISLR(dB) (range)	PSLR(dB) (azimuth)	ISLR(dB) (azimuth)
50	0 km	0.09	0.13	-13.3	-10.1	-13.3	-10.1
	0.5 km	0.09	0.13	-13.3	-10.1	-13.2	-10.1
	1 km	0.09	0.13	-13.2	-10.1	-12.2	-9.2
60	0 km	0.09	0.17	-13.3	-10.1	-13.3	-10.1
	0.5 km	0.09	0.17	-13.3	-10.1	-13.2	-10.1
	1 km	0.09	0.17	-13.3	-10.1	-12.1	-9.2
70	0 km	0.09	0.25	-13.2	-10.1	-13.1	-9.9
	0.5 km	0.09	0.25	-13.2	-10.1	-12.7	-9.6
	1 km	0.09	0.25	-13.2	-10.1	-12.6	-9.6

which is carried out directly with range uncompressed data. The second step is to define the phase error correction of range dependence. This step is carried out after the RCMC. In the high-squint case, the motion error is more complicated.

Based on the raw radar data, a motion compensation method was proposed in [21]. This dealt with the low-squint case with good results. The motion compensation method is already extended for the high-squint case [22] that may be applied to the imaging algorithm in this paper. The envelopment error is estimated and compensated for squint-minimized data without range compression. Then, the phase error would be estimated and compensated for the data after range compression [22]. This motion compensation method was valid by the data in the case of a squint of 50° and could obtain good focused SAR images.

3) Computational Load: This part mainly analyzes the computational load of this method. The parameters of the second simulation in Section IV are used. Supposing M and N denote the original azimuth and range sampling numbers, respectively, the range extension sampling number is about $N_{\text{ext}} = 1.14M$. $N_{\text{new}} = N_{\text{ext}} + N$ denotes the range sampling number after range extension. According to the flow of the ANCS-CS algorithm, the computational load can be written as

$$MN + 2M\frac{N}{2}\log_2 N + N\frac{M}{2}\log_2 M + 2M\frac{N_{\text{new}}}{2}\log_2 N_{\text{new}}$$
$$+ 3N_{\text{new}}\frac{M}{2}\log_2 M + 5MN_{\text{new}}. \quad (39)$$

In the NCS algorithm [19], spectrum expanding is needed to avoid aliasing [23]. The spectrum expanding results in increasing azimuth sampling number. By the aforementioned parameters, the new azimuth sampling number is about $M' = 1.95M$. The range extension needed in [19] can be expressed as $N_{\text{ext}} = 1.14M'$. Therefore, the computational load can be written as

$$M\frac{N}{2}\log_2 N + N\frac{M}{2}\log_2 M + 2NM' + M'\frac{N}{2}\log_2 N$$
$$+ 2M'\frac{N_{\text{new}}}{2}\log_2 N_{\text{new}} + 2N_{\text{new}}M' + N_{\text{new}}\frac{M'}{2}\log_2 M'. \quad (40)$$

Fig. 6 shows the variation of the computational time with scene dimension, where the original range and azimuth sampling

numbers are the same and a clock frequency of about 500 MHz is used. The abscissa denotes the scene dimension. From Fig. 6, we can see that the computational time is slightly less with our method than with the NCS algorithm.

IV. SIMULATION RESULTS

In this section, we provide some simulation results to demonstrate the performance of the proposed CS algorithms. The parameters for simulation are listed in Table II.

The simulations are performed under squint degrees of 50°, 60°, and 70°. From Table II, we can evaluate the ideal range and cross resolution $\rho_r = c/2B \cdot 0.886 = 0.0886$ m, $\rho_{\text{cross}} = D_a/2 \cdot 0.886 = 0.0886$ m, respectively, where B denotes the signal bandwidth and D_a is the azimuth aperture length. The ideal azimuth resolution, corresponding to squint angle θ_s, could be evaluated by $\rho_a = \rho_{\text{cross}}/\cos\theta_s$. Thus, the ideal azimuth resolutions are 0.138, 0.177, and 0.258 m under squint angles of 50°, 60°, and 70°, respectively. Note that the cross resolution is independent of the squint angle while the azimuth resolution is not. Four point targets are simulated under each squint angle; the range positions of each target are 0, 0.5, 1, and 2 km far away from the reference range, respectively. The reference range is $R_{\text{ref}} = 15$ km.

The quality parameters of the presented CS algorithm are listed in Table III. The range and azimuth resolutions tally well with the ideal resolution. Since there is no extra windowing operation, the theoretical values of peak and integrated sidelobe rations are about -13 and -10 dB, respectively. Note that the step of geometrical correction in the proposed CS algorithm is ignored here. Thus, the range and azimuth sidelobes seem perpendicular. We can see that the focusing of the proposed CS algorithm is good. The good performance is given by the squint minimization and ANCS, which highly increases the orthogonality between the range and azimuth of squinted data and reduces the space variance of the parameters of squinted data (Fig. 7).

In order to show the good performance of our method for range targets, we give two simulation results with a squint angle of 50°. Three range points are set in the scene. Their range coordinates are 0, 500, and 1000 m. The other parameters are the same as those in Table II. The NLCS algorithm [18] is used
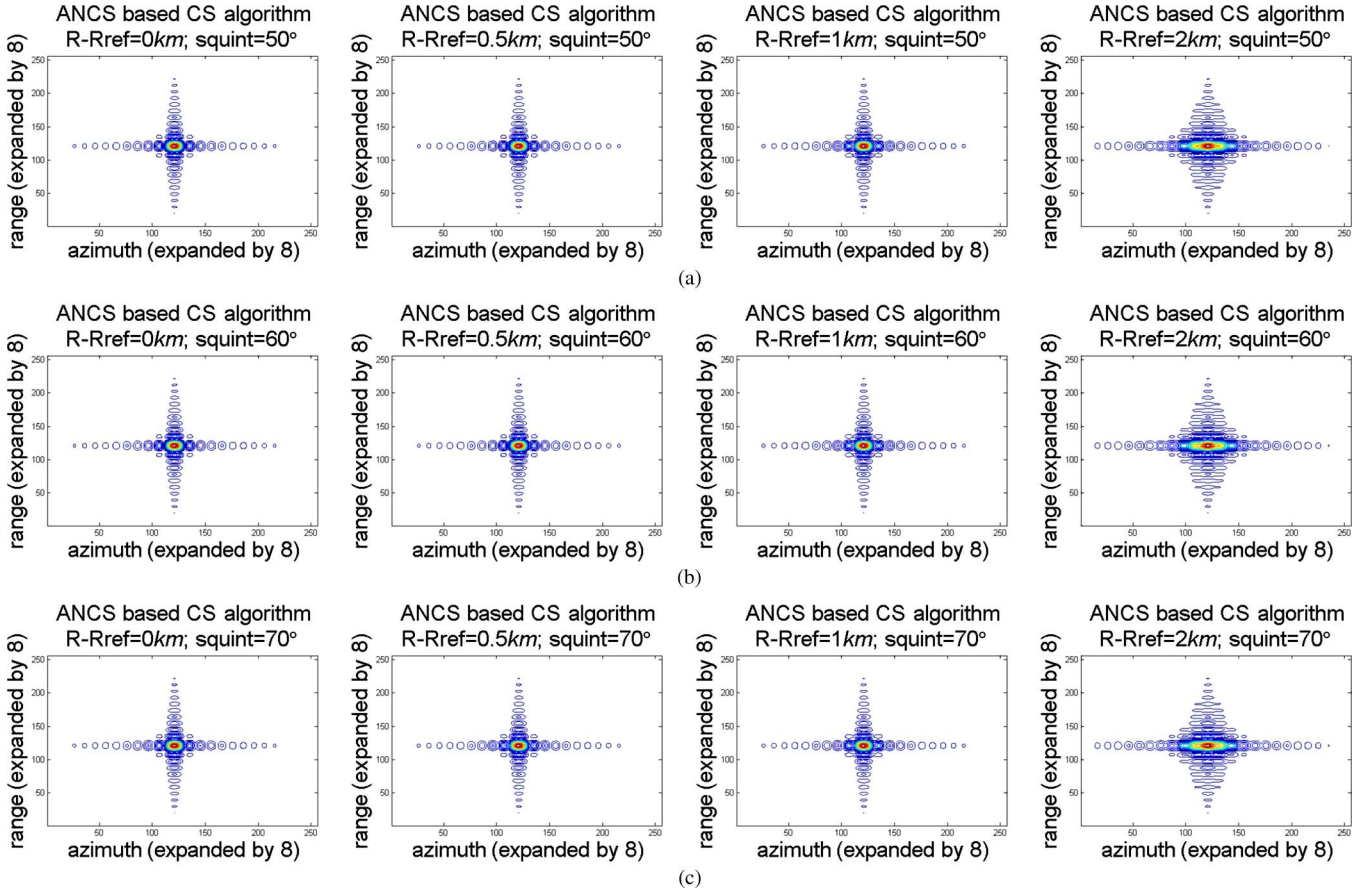
Fig. 7. Simulation results of the proposed CS algorithm. (a) Simulation results under a squint angle of 50°. (b) Simulation results under a squint angle of 60°. (c) Simulation results under a squint angle of 70°.

in comparison with our method. Figs. 8 and 9 show the results of the NLCS algorithm and the ANCS-based CS algorithm in this paper, respectively. The NLCS algorithm processes the data in the skew spectrum domain, while we adopt squint minimization to increase the degree of orthogonality between the range and azimuth. Hence, the RM, the space variance of RM and SRC terms, and the cubic phase term are much decreased via this step. However, for the reference point, the focusing results with a different algorithm are the same. With our method, the RCM of the farthest target is eliminated in Fig. 9(d), while the corresponding problem is not solved in NLCS. In addition, the space variance of the cubic phase term of range frequency will result in range defocusing, as seen in Fig. 8(d). The range defocusing will further affect the azimuth focusing results, and this can be seen in Fig. 8(b) and (c). From the following figures, we can conclude that our method is more suitable for focusing the range target.

Another simulation is presented here to show the advantage of our method over the method in [19]. In the simulation, the range and azimuth resolutions are both about 0.1 m, the wavelength is 0.01 m, the squint angle is about 70°, the reference range is 8000 m, and the speed of the platform is 100 m/s. Eight points in the reference range cell are simulated. The geometry of the eight points is shown in Fig. 10. The spaces of the neighbor points are 20, 20, 20, 20, 20, 50, and 50 m, respectively. In this simulation, the value of β_{scl} is 3. The range extension is needed according to the foregoing analysis. In this

simulation, the azimuth samplings are about 4368 and the range extension samplings are about 3830. Fig. 10(b1) and (b2) shows the azimuth focusing results of the fifth azimuth point with 100-m offset by using different methods. The sidelobe is much higher in the traditional method, while our focusing result is much better. The variations of the PLSR and ILSR with azimuth position are also studied. From Fig. 10(c1) and (c2), the PLSR and ILSR of our method vary a little while the PLSR and ILSR of the method in [19] rapidly deteriorate with azimuth position. So as to validate the azimuth distortion elimination without little main-lobe widening to different azimuth points, we study the ratio of main-lobe widening and azimuth distortion. We define the ratio of azimuth distortion as

$$RAD = \left| \frac{\overline{S_i S_{i-1}}}{\overline{S_2 S_1}} \frac{\overline{P_2 P_1}}{\overline{P_i P_{i-1}}} - 1 \right| \times 100\% \tag{41}$$

where $\overline{P_i P_{i-1}}$ denotes the line separation of P_i and P_{i-1} ($i = 2, 3, \ldots, 6$) and $\overline{S_i S_{i-1}}$ is the focused peak separation of P_i and P_{i-1} ($i = 2, 3, \ldots, 6$). From Fig. 10(c3), we see that our method is better in the high-squint case. Fig. 10(c4) shows that azimuth distortion is serious in the traditional method. Hence, azimuth interpolation is required to obtain the azimuth uniform space results. In the same condition, our method will not introduce the azimuth distortion without interpolation, which is one of the most significant advantages.
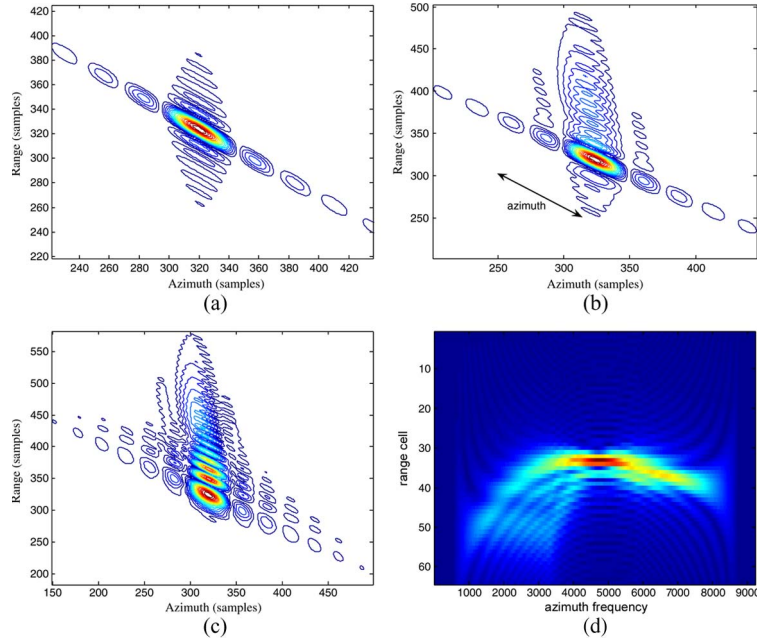
Fig. 8. Simulation results by using NLCS. (a)–(c) Focusing results of three range points, corresponding to 0, 500, and 1000 m, respectively. (d) Envelope of the farthest target.
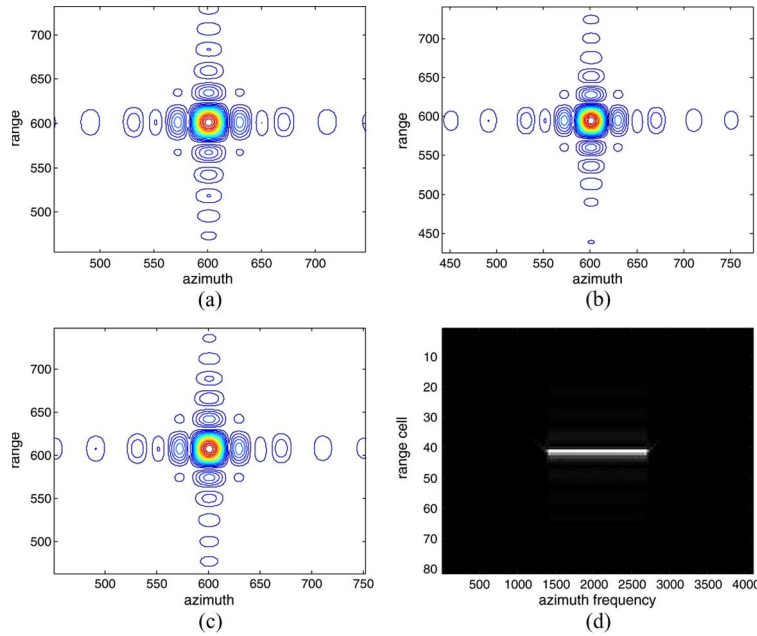
Fig. 9. Simulation results of our method. (a)–(c) Focusing results of three range points, corresponding to 0, 500, and 1000 m, respectively. (d) Envelope of the farthest target.

V. CONCLUSION

The highly squinted data are difficult to deal with due to their large RM, high space variance of focusing parameters, and large cubic phase terms. This arises from the lack of orthogonality between the range and azimuth of the squinted data. To accommodate for this, the squint-minimization operation is proposed in this paper. The proposed CS algorithm incorporates squint minimization with ANCS. Numerical examples guarantee the effectiveness of our proposed algorithm in high-resolution high-squint SAR imaging and also its advantage over other existing methods.

APPENDIX A
DERIVATION OF (35)

We start from (28) and rewrite the azimuth phase term after *azimuth cubic phase filtering*

$$S(t_m; R) = \exp\left[j\frac{b_m}{2}(t_m - \tau)^2 \right.$$
$$\left. + j\left(d'_m + \frac{d_m}{b_m^3} - \frac{d_0}{b_0^3} \right) b_m^3 (t_m - \tau)^3 \right]. \quad (A1)$$
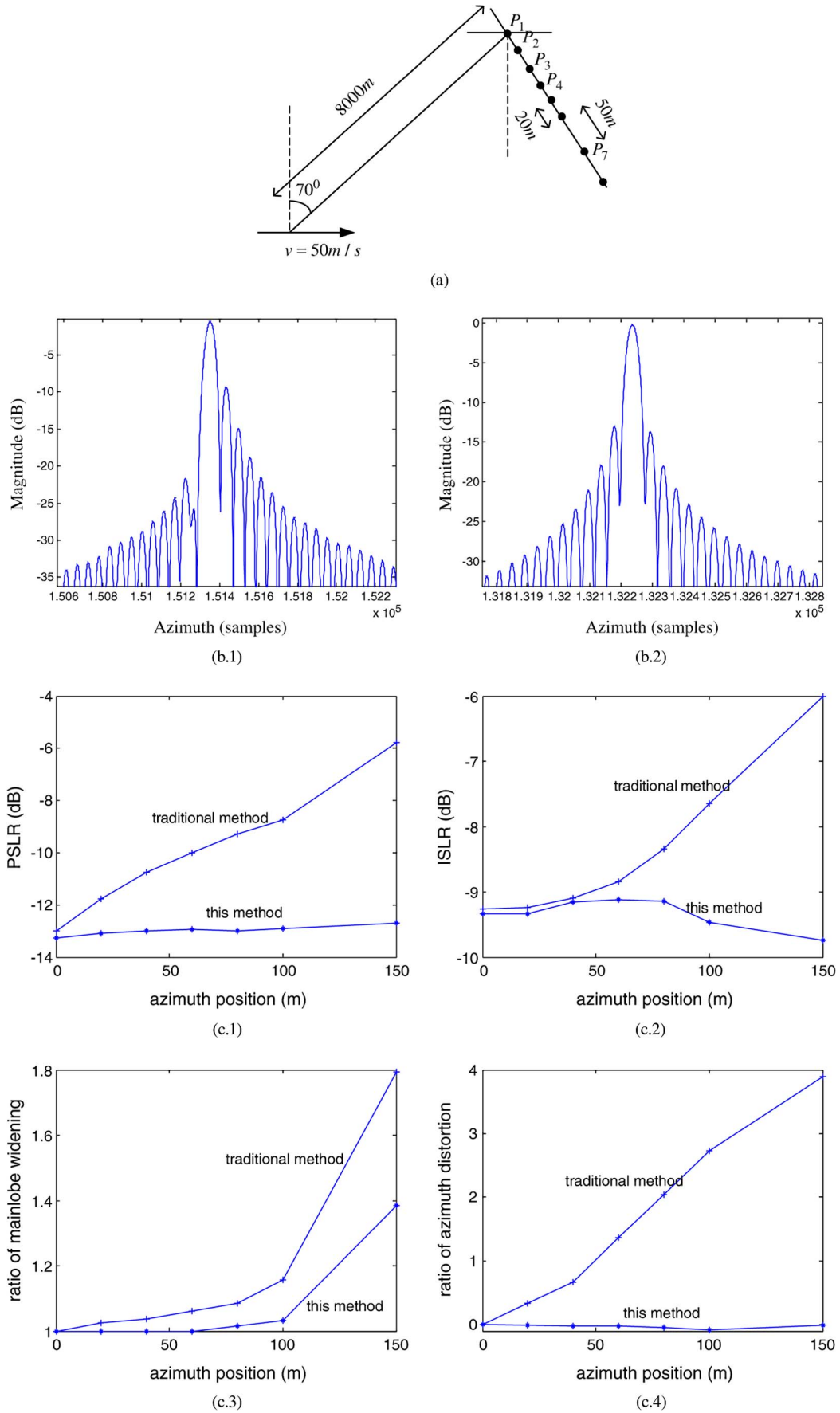
Fig. 10. Comparison of the current method and the method in [19]. (a) Geometry of eight points. (b1)–(b2) Comparison of the azimuth focusing results. (c1)–(c4) Performance comparison of the current method and the method in [19].

After multiplying the azimuth scaling term, (A1) is transformed to the azimuth frequency domain

$$S_1(f_a; R) = \int_{t_m} S(t_m; R) \exp\left(jq_2 t_m^2 / 2\right)$$

$$\times \exp\left(jq_3 t_m^3\right) \exp(-j2\pi f_a t_m) dt_m. \quad (A2)$$

By using the phase stationary method, we have

$$S_1(f_a; R) = \exp\left(j\Phi(f_a, \tau)\right) \quad (A3)$$

where

$$\Phi(f_a, \tau) = -2\pi f_a \frac{2\pi f_a + b_m \tau}{b_m + q_2} + \frac{1}{2(b_m + q_2)^2}$$

$$\times \left[b_m (2\pi f_a - q_2 \tau)^2 + q_2 (2\pi f_a + b_m \tau)^2\right]$$

$$+ \frac{1}{(b_m + q_2)^3}$$

$$\times \left[\left(d'_m + \frac{d_m}{b_m^3} - \frac{d_0}{b_0^3}\right) b_m^3 (2\pi f_a - q_2 \tau)^3 \right.$$

$$\left. + q_3 (2\pi f_a + b_m \tau)^3\right]. \quad (A4)$$

Equation (A4) is a little complicated. In order to express the azimuth distortion term and the azimuth FM term in position dependence, we rewrite (A4) in the following form:

$$\Phi(f_a, \tau) \approx A + B\tau f_a + C\tau^2 f_a + D\tau f_a^2 + E\tau f_a^3 \ldots \quad (A5)$$

where the parameters can be expressed in terms of the partial derivative of τ and f_a

$$A = \Phi(f_a, 0) \quad B = \frac{\partial^2 \Phi(0,0)}{\partial \tau \partial f_a} \quad C = \frac{\partial^3 \Phi(0,0)}{2\partial \tau^2 \partial f_a}$$

$$D = \frac{\partial^3 \Phi(0,0)}{2\partial \tau \partial f_a^2} \quad E = \frac{\partial^4 \Phi(0,0)}{6\partial \tau \partial f_a^3}. \quad (A6)$$

Equation (A4) consists of several fractional functions, which make the computations of (A6) more complicated. Therefore, we expand the parts of (A4)

$$\frac{1}{b_m + q_2} \approx \frac{1}{b_0 + q_2} - \frac{b_1}{(b_0 + q_2)^2}\tau$$

$$\frac{1}{(b_m + q_2)^3} \approx \frac{1}{(b_0 + q_2)^3} - \frac{3b_1 \tau}{(b_0 + q_2)^4} \quad (A7)$$

and arrive at

$$A = -\frac{2\pi^2}{b_0 + q_2} f_a^2 + \frac{8\pi^3 \left(d'_m b_0^3 + q_3\right)}{(b_0 + q_2)^3} f_a^3 \quad B = -\frac{2\pi b_0}{b_0 + q_2}$$

$$C = -\frac{2\pi b_1 q_2}{(b_0 + q_2)^2} + \frac{6\pi \left(q_3 b_0^2 + d'_m b_0^3 q_2^2\right)}{(b_0 + q_2)^3}$$

$$D = \frac{2\pi^2 b_1}{(b_0 + q_2)^2} + \frac{12\pi^2 \left(q_3 b_0 - d'_m q_2 b_0^3\right)}{(b_0 + q_2)^3}$$

$$E = \frac{48\pi^3}{(b_0 + q_2)^3} \left[3d'_m b_0^2 b_1 + \frac{d_0}{R}\right]. \quad (A8)$$

Let (34) be satisfied, and then, we obtain (35). From (A8) to (35), we adopt no approximation. Therefore, (35) has a high accuracy.

APPENDIX B
SELECTION OF β_{scl}

β_{scl} is the azimuth scaling factor. We do not want β_{scl} to be big. The bigger the value is, the smaller the focused map is in azimuth. However, in our simulation, the value of β_{scl} is greater than 1. Hence, β_{scl} has an optimal value to focus the scene point well and to obtain the smallest scaling result.

From Appendix A, we know that the azimuth dependence on the cubic phase term is not eliminated. However, by using our method, the azimuth dependence on the cubic phase term can be weakened. To analyze the new cubic phase term, we rewrite it as

$$\Phi_{3remain} = \frac{48\pi^3}{(b_0 + q_2)^3} \left[3d'_m b_0^2 b_1 + \frac{d_0}{R}\right] \tau f_a^3. \quad (B1)$$

Substituting (34) into (B1) leads to

$$\Phi_{3remain} = \frac{48\pi^3}{b_0^4 R \beta_{scl}^3 (\beta_{scl} - 1)}$$

$$\times \left[(\beta_{scl} - 0.5) b_1^2 R + (\beta_{scl} - 1) b_0 d_0\right] \tau f_a^3. \quad (B2)$$

Let

$$\varpi(\beta_{scl}) = \frac{48\pi^3}{b_0^4 R \beta_{scl}^3 (\beta_{scl} - 1)}$$

$$\times \left[(\beta_{scl} - 0.5) b_1^2 R + (\beta_{scl} - 1) b_0 d_0\right]. \quad (B3)$$

Then, $\varpi(\beta_{scl})$ is a function of squint range, squint angle, wavelength, and velocity of platform. In order to obtain the property of $\varpi(\beta_{scl})$, we have the logarithm plot of $\varpi(\beta_{scl})$ versus squint angle, with parameters the same as the second simulation in Section IV. From the plot (Fig. 11), we know that the bigger β_{scl} is, the smaller the azimuth dependence on the cubic phase term is. This is the same as our experience.

Usually, if the cubic phase term is limited by $\pi/4$, the error may be ignored. Then, β_{scl} can be obtained from the inequality

$$\varpi(\beta_{scl}) \tau f_a^3 < \pi/4 \quad (B4)$$

where f_a is confined in azimuth bandwidth and τ is restricted in the azimuth length of the scene. Equation (B4) is changed to

$$\varpi(\beta_{scl}) < 2\pi / \left(\tau_{max} B_a^3\right) \quad (B5)$$

where τ_{max} is the corresponding azimuth time of the scene edge point along azimuth.
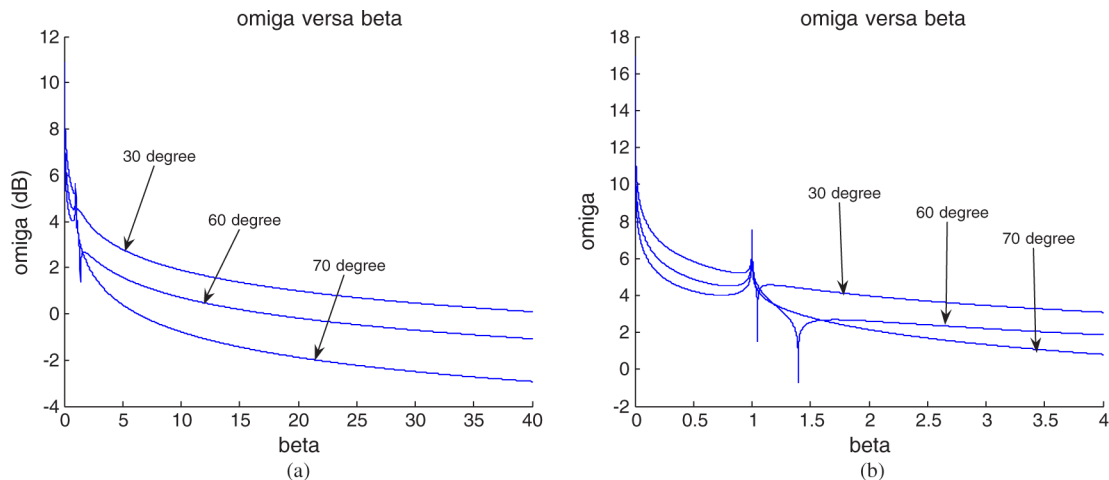
Fig. 11.   Plot of $\varpi(\beta_{\mathrm{sc1}})$ versa β_{sc1}. (a) Plots with different squint angles. (b) Local plots of (a).

ACKNOWLEDGMENT

The authors would like to thank the Associate Editor and the anonymous reviewers, whose suggestions are valuable in improving the manuscript.

REFERENCES

[1] J. R. Bennett and I. G. Cumming, "A digital processor for the production of SeaSat synthetic aperture radar imagery," in *Proc. SURGE Workshop*, Frascati, Italy, 1979, ESA-SP-154.

[2] M. Y. Jin and C. Wu, "A SAR correlation algorithm which accommodates large range migration," *IEEE Trans. Geosci. Remote Sens.*, vol. GRS-22, no. 6, pp. 592–597, Nov. 1984.

[3] C. Y. Chang, M. Jin, and J. C. Curlander, "Squint mode SAR processing algorithms," in *Proc. IGARSS*, Vancouver, BC, Canada, 1989, pp. 1702–1706.

[4] F. H. Wong and I. G. Cumming, "Error sensitivities of a secondary range compression algorithm for processing squinted satellite SAR data," in *Proc. IGARSS*, Vancouver, BC, Canada, 1989, pp. 2584–2587.

[5] A. M. Smith, "A new approach to range–Doppler SAR processing," *Int. J. Remote Sens.*, vol. 12, no. 2, pp. 235–251, Feb. 1991.

[6] A. R. Schimidt, "Secondary range compression for improved range Doppler processing of SAR data with high squint," M.S. thesis, Univ. British Columbia, Vancouver, BC, Canada, Sep., 2008.

[7] F. Rocca, "Synthetic aperture radar: A new application for wave equation techniques," Stanford Exploration Project, Stanford, CA, Rep. SEP-56, pp. 167–189, 1987.

[8] F. Rocca, C. Prati, and A. M. Guarnieri, "New algorithms for processing of SAR data," ESA, Frascati, Italy, ESA Contract Rep., ESRIN Contract no.7998/88/F/FL(SC), 1989.

[9] C. Cafforio, C. Prati, and F. Rocca, "SAR data focusing using seismic migration techniques," *IEEE Trans. Aerosp. Electron. Syst.*, vol. 27, no. 2, pp. 194–207, Mar. 1991.

[10] R. Bamler, "A comparison of range–Doppler and wave-number domain SAR focusing algorithms," *IEEE Trans. Geosci. Remote Sens.*, vol. 30, no. 4, pp. 706–713, Jul. 1992.

[11] G. Franceschetti, R. Lanari, V. Pascazio, and G. Schirinzi, "WASAR: A wide-angle SAR processor," *Proc. Inst. Elect. Eng.*, vol. 139, pt. F, no. 2, pp. 107–114, Apr. 1992.

[12] R. K. Ranev and P. W. Vachon, "A phase preserving SAR processor," in *Proc. IGARSS*, Vancouver, BC, Canada, 1989, pp. 2588–2591.

[13] R. H. Stolt, "Migration by Fourier transform," *Geophysics*, vol. 43, no. 1, pp. 23–48, Feb. 1978.

[14] A. Papoulis, *Systems and Transforms With Applications in Optics*.   New York: McGraw-Hill, 1968.

[15] R. K. Raney, H. Runge, R. Bamler, I. G. Cumming, and F. H. Wong, "Precision SAR processing using chirp scaling," *IEEE Trans. Geosci. Remote Sens.*, vol. 32, no. 4, pp. 786–799, Jul. 1994.

[16] A. Moreira and Y. Huang, "Airbome SAR processing of highly squinted data using a chirp scaling approach with integrated motion compensation," *IEEE Trans. Geosci. Remote Sens.*, vol. 32, no. 5, pp. 1029–1040, Sep. 1994.

[17] A. Moreira, J. Mittermayer, and R. Scheiber, "Extended chirp scaling algorithm for air- and spaceborne SAR data processing in stripmap and ScanSAR imaging modes," *IEEE Trans. Geosci. Remote Sens.*, vol. 34, no. 5, pp. 1123–1136, Sep. 1996.

[18] G. W. Davidson, I. G. Cumming, and M. R. Ito, "A chirp scaling approach for processing squint mode SAR data," *IEEE Trans. Aerosp. Electron. Syst.*, vol. 32, no. 1, pp. 121–133, Jan. 1996.

[19] F. H. Wong and T. S. Yeo, "New applications of nonlinear chirp scaling in SAR data processing," *IEEE Trans. Geosci. Remote Sens.*, vol. 39, no. 5, pp. 946–953, May 2001.

[20] C. Y. Chang, M. Y. Jin, and J. C. Curlander, "SAR processing based on the exact two-dimensional transfer function," in *Proc. IGARSS*, 1992, pp. 355–359.

[21] M. Xing, X. Jiang, R. Wu, F. Zhou, and Z. Bao, "Motion compensation for UAV SAR based on raw radar data," *IEEE Trans. Geosci. Remote Sens.*, vol. 47, no. 8, pp. 2870–2883, Aug. 2009.

[22] F. Zhou, Q. Wan, M. Xing, and Z. Bao, "A novel method of motion compensation for airborne high squint synthetic aperture radar," *Acta Electron. Sin.*, vol. 35, no. 3, pp. 463–468, Mar. 2007.

[23] G. W. Davidson and I. Cumming, "Signal properties of spaceborne squint-mode SAR," *IEEE Trans. Geosci. Remote Sens.*, vol. 35, no. 3, pp. 611–617, May 1997.

[24] A. Moreira, R. Scheiber, and J. Mittermayer, "Azimuth and range scaling for SAR and ScanSAR processing," in *Proc. IGARSS*, 1996, pp. 1214–1216.

[25] P. Berens, "Efficient wave number domain processing for squinted spotlight SAR," in *Proc. EUSAR*, 2004, pp. 171–174.

[26] M. Vandewal, R. Speck, and H. Suess, "Efficient and precise processing for squinted spotlight SAR through a modified Stolt mapping," *EURASIP J. Adv. Signal Process.*, vol. 2007, pp. 1–7, 2007.
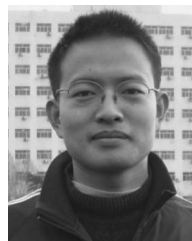
Guangcai Sun was born in Hubei, China, in December 1984. He received the B.S. degree in communications engineering from Post and Telecommunication Institution, Xi'an, China, in 2006. He is currently working toward the Ph.D. degree in the National Key Laboratory of Radar Signal Processing, Xidian University, Xi'an.

His research interests include synthetic aperture radar imaging and moving target detection.
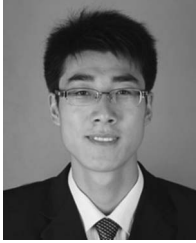
Xiuwei Jiang was born in Shandong, China, in February 1986. He received the B.S. degree in electrical engineering from Xidian University, Xi'an, China, in 2007, where he also received the M.S. degree in the National Key Laboratory of Radar Signal Processing, under the guide of Dr. Mengdao Xing.

His current research interests include synthetic aperture radar (SAR), inverse SAR, and signal processing.

Mengdao Xing (S'00–A'03–M'04) was born in Zhejiang, China, in November 1975. He received the B.S. and Ph.D. degrees in electrical engineering from Xidian University, Xi'an, China, in 1997 and 2002, respectively.

He is currently a Full Professor with the National Key Laboratory of Radar Signal Processing, Xidian University. He is also with the National Key Laboratory of Microwave Imaging Technology, Institute of Electronics, Chinese Academy of Sciences, Beijing, China. His research interests include synthetic aperture radar (SAR), inverse SAR, and over-the-horizon radar.

Zhi-jun Qiao received the Ph.D. degree in applied math from the Institute of Mathematics, Fudan University, Shanghai, China, in 1997, wherein his dissertation was one of the first 100 excellent Ph.D. dissertations awarded in 1999.

From 1999 to 2001, he was a Humboldt Research Fellow with the Department of Mathematics and Computer Science, University of Kassel, Germany. From 2001 to 2004, he was a Researcher with the Theoretical Division, Los Alamos National Laboratory. He was also a Professor with the Department of Mathematics, Liaoning University, Shenyang City, China, in 1997. Currently, he is the PI of two grants under the Department of Defense program and the Norman Hackerman Advanced Research Program. He is currently with the Department of Mathematics, The University of Texas-Pan American, Edinburg. He is currently the Editor-in-Chief of the *Pacific Journal of Applied Mathematics*. He has published two monographs and more than 90 articles in peer-reviewed international journals.

Yirong Wu (M'00) received the M.S. degree from the Beijing Institute of Technology, Beijing, China, in 1988 and the Ph.D. degree from the Institute of Electronics, Chinese Academy of Sciences (IECAS), Beijing, in 2001.

Since 1988, he has been with IECAS, where he currently serves as the Director. He has over 20 years of experience in remote-sensing processing system design. His current research interests are microwave imaging, signal and information procession, and related applications.

Zheng Bao (M'80–SM'90) was born in Jiangsu, China. He received the B.S. degree from the Communication Engineering Institute of China (currently Xidian University), Xi'an, China, in 1953.

He is currently a Professor and the Chairman of the Academic Board of the National Key Laboratory of Radar Signal Processing, Xidian University. He is the author or a coauthor of six books and more than 300 papers. His current research fields include space–time adaptive processing, radar imaging (synthetic aperture radar (SAR)/inverse SAR), automatic target recognition, and over-the-horizon radar signal processing.

Prof. Bao is a member of the Chinese Academy of Sciences.